



Originally published as:

Mohsen, A., Hofstetter, R., Bock, G., Kind, R., Weber, M., Wylegalla, K., Rämpker, G., DESERT Group (2005): A receiver function study across the Dead Sea Transform. - Geophysical Journal International, 160, 3, pp. 948—960.

DOI: <http://doi.org/10.1111/j.1365-246X.2005.02534.x>

# A receiver function study across the Dead Sea Transform

A. Mohsen,<sup>1,2</sup> R. Hofstetter,<sup>3</sup> G. Bock,<sup>1,\*</sup> R. Kind,<sup>1,4</sup> M. Weber,<sup>1,5</sup>  
K. Wylegalla,<sup>1</sup> G. Rümper<sup>1,5</sup> and the DESERT Group

<sup>1</sup>GFZ, 14473 Potsdam, Germany

<sup>2</sup>Al-Najah National University, Nablus, Palestine

<sup>3</sup>Geophysical Institute, Lod, Israel

<sup>4</sup>Freie Universität, Berlin, Germany

<sup>5</sup>Universität Potsdam, Germany

Accepted 2004 November 23. Received 2004 November 16; in original form 2004 January 20

## SUMMARY

We report on a receiver function study of the crust and upper mantle within DESERT, a multidisciplinary geophysical project to study the lithosphere across the Dead Sea Transform (DST). A temporary seismic network was operated on both sides of the DST between 2000 April and 2001 June. The depth of the Moho increases smoothly from about 30 to 34–38 km towards the east across the DST, with significant north–south variations east of the DST. These Moho depth estimates from receiver functions are consistent with results from steep- and wide-angle controlled-source techniques. Steep-angle reflections and receiver functions reveal an additional discontinuity in the lower crust, but only east of the DST. This leads to the conclusion that the internal crustal structure east and west of the DST is different. The *P* to *S* converted phases from both discontinuities at 410 and 660 km are delayed by 2 s with respect to the IASP91 global reference model. This would indicate that the transition zone is consistent with the global average, but the upper mantle above 410 km is 3–4 per cent slower than the standard earth model.

**Key words:** crustal structure, Dead Sea Transform, mantle discontinuities.

## INTRODUCTION

The Dead Sea Transform (DST) is one of the most significant geological structures in the Middle East (Quennell 1958; Wilson 1965; Freund *et al.* 1970; McKenzie *et al.* 1970; McKenzie 1972). It separates the Arabian and African plates, strikes in a north-northeast direction and extends over some 1000 km from the active spreading centre of the Red Sea, along the Wadi Araba, Dead Sea, Jordan Valley, Lake Tiberias and central Lebanon to the continental collision zone in the Taurus–Zagros mountain belt (McKenzie *et al.* 1970; Garfunkel 1981; Girdler 1990; El-Isa 1990; Kovach *et al.* 1990) (Fig. 1). From geological field observations it is estimated that about 105 km of horizontal movement has occurred since it began to form in the Cenozoic about 20 Ma (Quennell 1958; Freund *et al.* 1970; Garfunkel 1981; Girdler 1990).

The DESERT Project, a multinational geophysical project, has imaged the structure of the lithosphere across the DST from the Mediterranean to Jordan between the Dead Sea and the Red Sea. It included a number of controlled and natural source seismic experiments. The experiments and first results have been described in

DESERT Group (2000, 2004), Rümper *et al.* (2003), Sobolev *et al.* (2004), Koulakov *et al.* (2004), Mechie *et al.* (2004) and Haberland *et al.* (2003). Here we describe a receiver function analysis of teleseismic records in terms of crustal and upper mantle structure and compare the results with the controlled-source results.

## RECEIVER FUNCTION TECHNIQUE

We applied the receiver function technique to determine the thickness of the crust, the average crustal  $V_p/V_s$  ratio and the differential times of the 410 and 660 discontinuities. The background of the receiver function technique has been reported in a number of papers (e.g. Vinnik 1977; Burdick & Langston 1977; Owens *et al.* 1984; Ammon *et al.* 1990; Langston 1994; Zandt & Ammon 1995; Nyblade *et al.* 2000; Owens *et al.* 2000) and it has successfully been applied for example in Germany (Kind *et al.* 1995; Grunewald *et al.* 2001), in Tibet (Yuan *et al.* 1997; Kosarev *et al.* 1999; Kind *et al.* 2002), in the Middle East (Hofstetter & Bock 2004), in the Middle East and North Africa (Sandvol *et al.* 1998), in North America (e.g. Ramesh *et al.* 2002) and in the Andes (Yuan *et al.* 2000, 2002). A very valuable feature of the receiver function technique is the use of crustal multiples for determination of accurate crustal thicknesses and average  $V_p/V_s$  ratios (Zandt *et al.* 1995; Zhu & Kanamori 2000).

\* Deceased (2002 November 6).

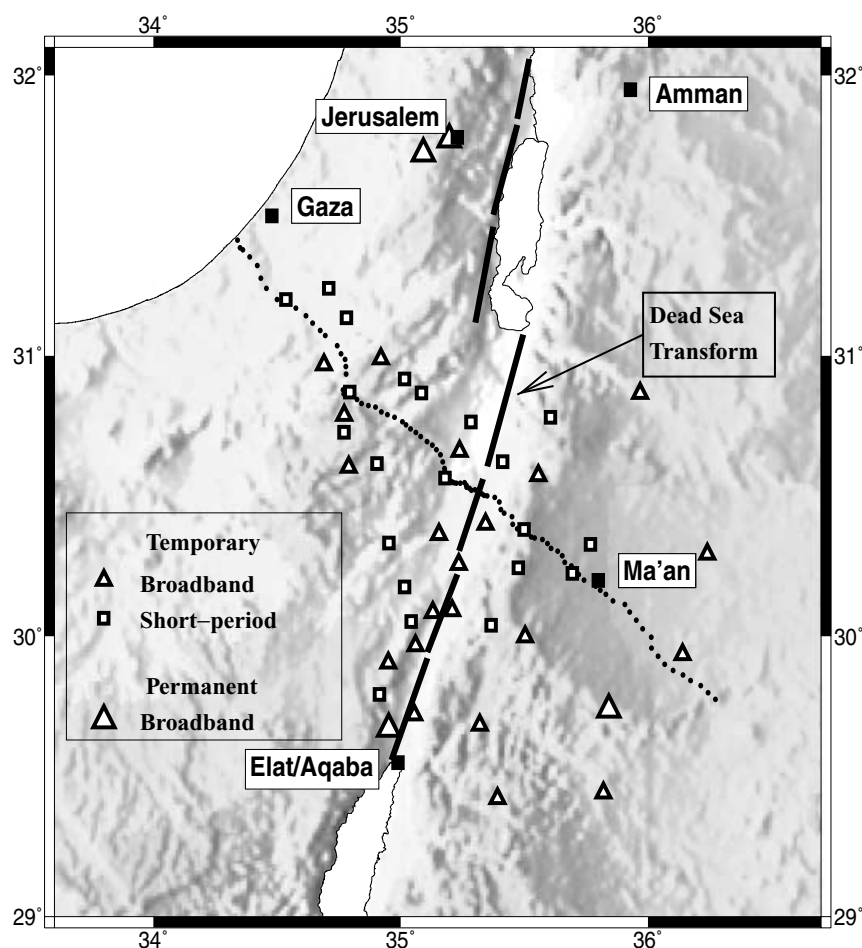


**Figure 1.** Location map of seismic stations in the region of the Dead Sea Transform (DST). Locations of permanent broadband stations and of temporary broadband and short-period stations of the DESERT project are shown. The dotted line shows the steep- and wide-angle controlled-source profiles discussed in DESERT Group (2000, 2004).

The usual processing is: rotation of the three components Z–N–E into the local ray coordinate system  $P$ – $SV$ – $SH$  (Kind *et al.* 1995), deconvolution of the  $SV$  component by the  $P$  component, distance move-out correction for direct conversions at a standard slowness of 6.4 s per degree and summation (Yuan *et al.* 1997). In addition we applied a bandpass filter between 3 and 20 s to improve the signal-to-noise ratio. The distribution of the earthquake recording stations is shown in Fig. 1, along with the location of the controlled-source seismic line (DESERT Group 2004). Seismological stations operated between 2000 April and 2001 June. Twenty-one broadband and 21 short period (1 Hz) seismometers have been used. Longer periods recorded by the short-period instruments have been restituted (Yuan *et al.* 1997). The data were continuously recorded with a sampling rate of 50 samples per second. The aperture of the network is approximately 250 km in the northwest–southeast direction and 150 km in the southwest–northeast direction. It covers the territories of Palestine, Israel and Jordan. The data are in the archive of the GEO-FON network at the GFZ in Potsdam, Germany. The coordinates of the stations used are listed in Table 1. About 92 useful teleseismic events were selected with epicentral distances ranging from 30° to 90° and magnitudes greater than 5.5. The epicentres of the events are displayed in Fig. 2. Most of the events by far are in the northeast quadrant.

## MOHO DEPTH AND CRUSTAL $V_p/V_s$ RATIO

Fig. 3 shows summed receiver functions of all stations (see Fig. 4 for the location of stations and piercing points at 33 km depth). Several phases are easily identified in the traces in Fig. 3. The first one is a conversion labelled ‘sediments’, which originates from a strong contrast in the upper crust. Stations on crystalline basement like JS07 and JW09 in Fig. 3B (at the bottom) do not have this phase. The second one is the conversion from the Moho. In addition we see crustal multiples. The records in Fig. 3 are grouped according to the appearance of their multiples. Group A has one clear Moho multiple, which has two additional  $P$  legs in the crust. Group B has the same Moho multiple plus an additional multiple, which is very probably caused by a discontinuity in the lower crust (as will be shown later). Group C has no coherent visible multiples. The spatial distribution of the members of the three groups is shown in Fig. 4. Group A has, with one exception (JS02), only stations west of the DST whereas group B, again with one exception (ID16), has only stations on or to the east of the DST.

We have used the crustal multiples for determination of crustal thickness  $H$  and average  $V_p/V_s$  ratio. This was done using two methods. First we used the Zhu & Kanamori (2000) method. This method

**Table 1.** Station codes, coordinates and elevations of earthquake stations of the DESERT project.

ID	Latitude	Longitude	Elevation (m)
ID02	31.24	34.71	255
ID01	31.20	34.54	165
ID03	31.14	34.78	305
ID12	30.99	34.92	505
ID26	30.97	34.69	365
ID05	30.87	34.79	505
ID15	30.87	35.08	110
ID07	30.79	34.77	580
ID04	30.73	34.77	725
ID17	30.62	34.90	470
ID08	30.60	34.79	870
ID21	30.33	34.95	290
JS01	30.29	36.24	880
ID16	30.92	35.02	400
JW01	30.87	35.97	885
JK01	30.78	35.61	1400
ID19	30.77	35.28	135
ID27	30.66	35.24	65
ID06	30.56	35.18	20
ID28	30.36	35.16	130
JD05	30.26	35.23	400
JK05	30.24	35.48	1680
JW05	30.23	35.69	1200
JD06	30.09	35.21	300
ID31	30.08	35.13	225
ID32	29.97	35.06	145
JS03	29.94	36.14	935
JW09	29.68	35.32	835
JS07	29.42	35.39	1130
JD03	30.62	35.41	145
JK02	30.57	35.56	1200
JD04	30.40	35.34	300
JK04	30.38	35.50	1750
JW04	30.33	35.77	1100
ID22	30.18	35.02	310
ID23	30.05	35.04	445
JK06	30.04	35.37	1140
JW07	30.00	35.50	1650
ID33	29.90	34.95	570
ID24	29.79	34.91	870
JD08	29.72	35.05	225
JS05	29.44	35.82	930

performs a grid search through the  $H$  and  $V_p/V_s$  space and searches for the largest summed amplitudes at the predicted times of direct conversions and multiples. The second approach was to measure visually the times of the direct conversion and of the  $PP$  multiple. Table 2 lists the  $H$  and  $V_p/V_s$  values of each technique and their differences (only groups A and B; for group C only the technique of Zhu & Kanamori 2000, was applicable). At 14 stations the difference in  $H$  is less than 1 km, at 14 stations it is 1 km, and at two stations 2 km. The difference in the  $V_p/V_s$  ratio is at 26 stations less than or equal to 0.03, at one station it is 0.40, and at three stations it is between 0.05 and 0.17. If the  $V_p/V_s$  ratio was smaller than 1.71 or larger than 1.85 we used the average value of 1.77 instead (at two stations of group B and four stations of group C; see Table 2).

In both methods we need to prescribe the average  $P$  velocity of the crust. However,  $H$  and  $V_p/V_s$  determinations are not very sensitive to  $V_p$  variations, the resulting Moho depths  $H$  versus  $V_p/V_s$  ratios from Table 2 (using the technique of Zhu & Kanamori 2000, including corrected values, marked by a star in Table 2) are plotted for a  $V_p$

of  $6.1 \text{ km s}^{-1}$ . A number of  $H-V_p/V_s$  pairs are double and thus we have fewer values in Fig. 5 than in Table 2. We have also used  $V_p$  values of 6.0 and  $6.2 \text{ km s}^{-1}$  to estimate the possible errors in  $H$  and  $V_p/V_s$ . The crustal thickness  $H$  changes by about 0.6 km and the  $V_p/V_s$  ratio by less than 0.01, if  $V_p$  is changed by  $0.1 \text{ km s}^{-1}$ . These changes are shown in Fig. 5 for one station, but they are very similar for all other  $H-V_p/V_s$  pairs. We conclude from these considerations that the absolute errors in the Moho depth determinations are close to  $\pm 1 \text{ km}$ , and  $\pm 0.01$ – $0.02$  for the average crustal  $V_p/V_s$  ratios.

In Figs 6 and 7 we have mapped the Moho depths and the  $V_p/V_s$  ratios from Fig. 5 and Table 2 (using the technique of Zhu & Kanamori 2000). The obtained Moho depths range from 31 to 37 km. At 11 stations the Moho is deeper than 34 km. These stations are all located on the DST or to the east of it (blue colours in Fig. 6). East of the DST, Moho depths are greatest beneath the central portion of the network and shallower towards the northern and southern ends of the network. This means that the Moho east of the DST forms a trough-like feature with the deepest parts exactly where the controlled-source profile is located (dotted line in Fig. 6). Moho depths west of the DST are practically all 33 km or less. There are no clear systematics in the distribution of the  $V_p/V_s$  ratios in Fig. 7, although in Fig. 5 the  $V_p/V_s$  ratios seem to form in two groups with one group having values smaller than 1.76 and the other having values larger than 1.79. Larger values are somewhat more frequent west of the DST. Moho depths larger than 34 km seem to have  $V_p/V_s$  ratios close to about 1.76, and extremely large  $V_p/V_s$  ratios are not observed at large Moho depths (see Fig. 5).

## A LOWER CRUSTAL DISCONTINUITY EAST OF THE DST

Group B in Fig. 3 has a clear additional signal between the Moho conversion and the Moho multiple, labelled LCM (lower crustal multiple). It is very likely that this phase is a multiple since it clearly arrives parallel to the Moho multiple (Fig. 3B). In Fig. 8 we invert the waveforms of one station of group A (ID08) and one station of group B (JW05). We are not using an inversion technique as suggested by Kind *et al.* (1995). Such an inversion technique may fit the waveform nearly perfectly but results in very complicated, often oscillatory, 1-D models. We search instead by forward modelling for simple models where each significant phase can be identified, although the waveform fit might not be as perfect as in the inversion. The top three panels in Fig. 8 (A, B and C) show the modelling of the waveforms of station JW05. Panel A compares computed waveforms (continuous line) of a sedimentary layer over a granitic half-space with the observed waveforms (dashed line). Whereas the computed and observed times of the conversion at the base of the sediments agree well, the computed amplitude is too small. We do not try to fit this amplitude with a 1-D model, since we think 3-D structure plays an important role. In panel B we add a lower crustal discontinuity, which produces a direct conversion, which has amplitudes which are too small compared with the observations. However, it also produces a multiple, which exactly fits an observed phase, which we therefore interpret as a multiple of the lower crustal discontinuity. The fact that the controlled-source experiment (DESERT Group 2004) mapped such a reflector guided us in developing such a model. In panel C we add the Moho, which fits the observed signal near 5 s very well, together with the lower crustal conversion. The Moho multiples also fit later parts of the signal very well. What we call the Moho conversion in group B is indeed a superposition of a conversion from the lower crust and the Moho. The two directly

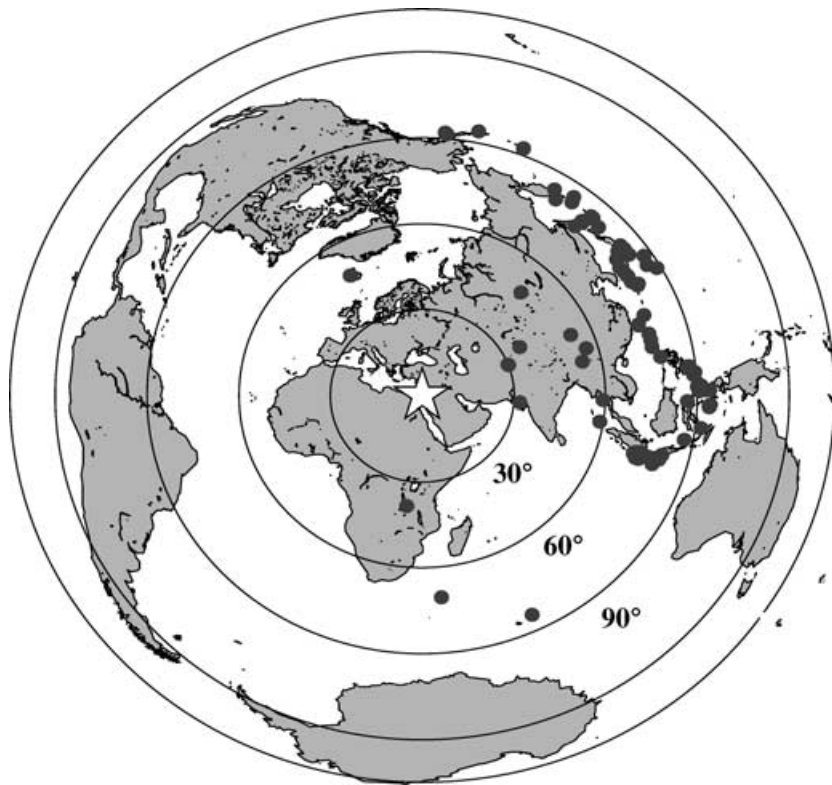


**Figure 2.** Distribution of teleseismic events with magnitude greater than 5.5 used in this study for receiver function analysis. The equidistant circles show distance to the DESERT network in the Middle East in degrees.

converted phases cannot be separated due to their relatively long periods and small differential times. The multiples of both phases, however, are clearly separated. In Fig. 9 we have mapped the depth location of the lower crustal discontinuity east of the DST. As in the Moho depth map in Fig. 6 the lower crustal discontinuity is deepest near the WRR profile except for station JS03. At the northern and southern ends of the station network, the lower crustal discontinuity is shallower again.

#### COMPARISON OF RESULTS FROM NATURAL AND CONTROLLED-SOURCE TECHNIQUES

Several controlled-source seismic experiments have been carried out within the DESERT project (DESERT Group 2000). One of them was a 260 km long wide-angle profile from the Mediterranean across Palestine and Israel into Jordan, coinciding across the DST with a 100 km long steep angle reflection profile (see Fig. 1). Some controlled-source seismic experiments and their results are discussed in DESERT Group (2004). The wide-angle data show a continuous increase in the Moho depth from about 27 km at the coast to about 40 km at the end of the profile in Jordan (DESERT Group 2004). In the region of overlap, the near vertical reflection results confirm the wide-angle results. Our natural source data show practically the same picture for the crustal thickness (Fig. 10). However, we did not succeed in obtaining earthquake data from stations near the Mediterranean coast, where controlled-source data indicate a Moho depth well below 30 km. West of the DST our Moho deepens from 31 km to about 35 km below the DST, and continues to deepen to nearly 40 km at the easternmost stations. However, we observe this continuous deepening of the Moho from west to east

only along the controlled-source profile. East of the DST the natural source data indicate a shallower Moho to the north and south than directly along the controlled-source line (reaching values of 33 km, see Fig. 11). This observation indicates that the continuous deepening of the Moho from west to east across the DST is only a local feature, and does not exist everywhere east of the DST. The Moho to the north and south of the controlled-source line east of the DST seems to have similar depths as west of the DST. The controlled-source line was located by chance in a Moho trough east of the DST.

An interesting feature in the near vertical reflection data is a lower crustal reflector rising from the Moho at the DST to less than 30 km depth towards the east. The near vertical reflection data do not show such feature in the western part of the DST. The natural source data confirm the existence of this lower crustal discontinuity (LCD) at and to the east of the DST. It is located in the same depth range as determined by the controlled-source data. This discontinuity also shallows north and south of the controlled-source line, to values of 21–25 km (Fig. 11).

#### THE MANTLE TRANSITION ZONE

The receiver function technique usually also observes signals from the upper mantle discontinuities at 410 and 660 km depth (e.g. Vinnik 1977; Nyblade *et al.* 2000; Owens *et al.* 2000; Li *et al.* 2003). These discontinuities are considered to be primarily due to phase transformations in the olivine system (see Helffrich 2000 for a review). Thus the actual depth locations of these discontinuities is temperature and pressure dependent. However, variations in the delay time of the 410 km conversion predominantly indicate changes in the average upper mantle velocity. Variations in the differential

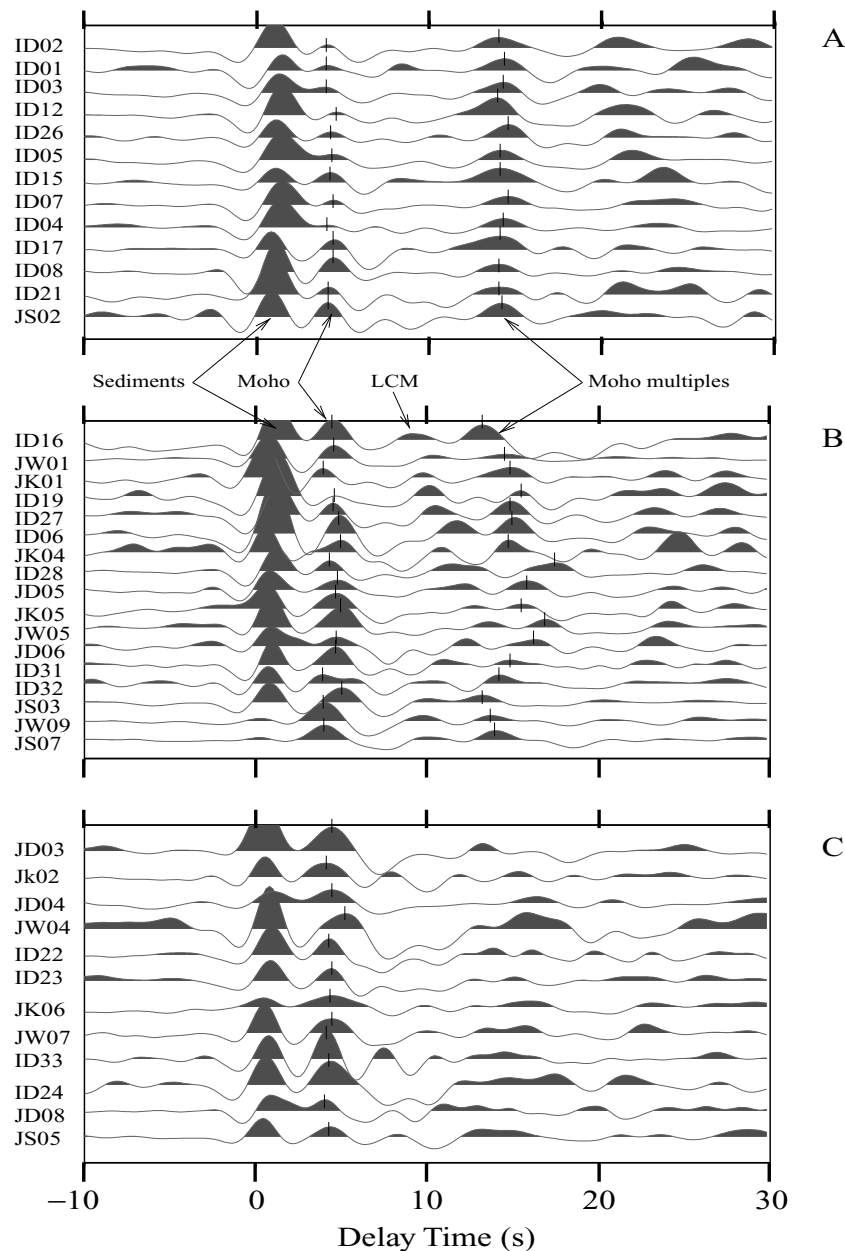


**Figure 3.** Summed receiver functions for each station. Conversions from an upper crustal discontinuity ('sediments'), from the Moho and crustal multiples are visible. Stations are grouped according to the appearance of their multiples. Group A has one clear multiple, group B has besides the Moho multiple an additional multiple from a discontinuity in the lower crust (LCM). Group C has no clearly visible multiples.

time of the two discontinuities indicate mainly thickness changes of the transition zone, which are indications of temperature variations at that depth (Li *et al.* 2003).

Fig. 12 shows the signals from both upper mantle discontinuities. The traces are plotted according to the longitude of their piercing points at 660 km depth from west to east. Fig. 13 shows the distribution of the piercing points of both discontinuities. Practically all of them are east or northeast of the DST covering the territory of Jordan. This means we do not have information from the upper mantle or the transition zone across the DST. Traces in Fig. 12 are summed over a window of  $1^\circ$  and plotted. This window is moved by  $0.2^\circ$  and a new summation trace is created. All traces are summed and plotted at the top of Fig. 12. The quality of the upper mantle

conversions is not very high. In the summation trace, however, the 410 and 660 km conversions are visible. Before summation a distance move-out correction is applied, using the IASP91 model and a reference slowness of 6.4 s per degree permitting summation of records from different distances. The arrival time of the 410 km signal is 45.6 s, and the differential time for both discontinuities is 24.2 s. IASP91 values are 44.0 and 24.0 s, respectively. This means that the upper mantle east of the DST is 3–4 per cent slower than the global average and the thickness of the transition zone is close to the global average. To study the upper mantle across the DST with receiver functions we would need to install stations further to the southwest, in the Sinai, since most events arrive from the northeast.

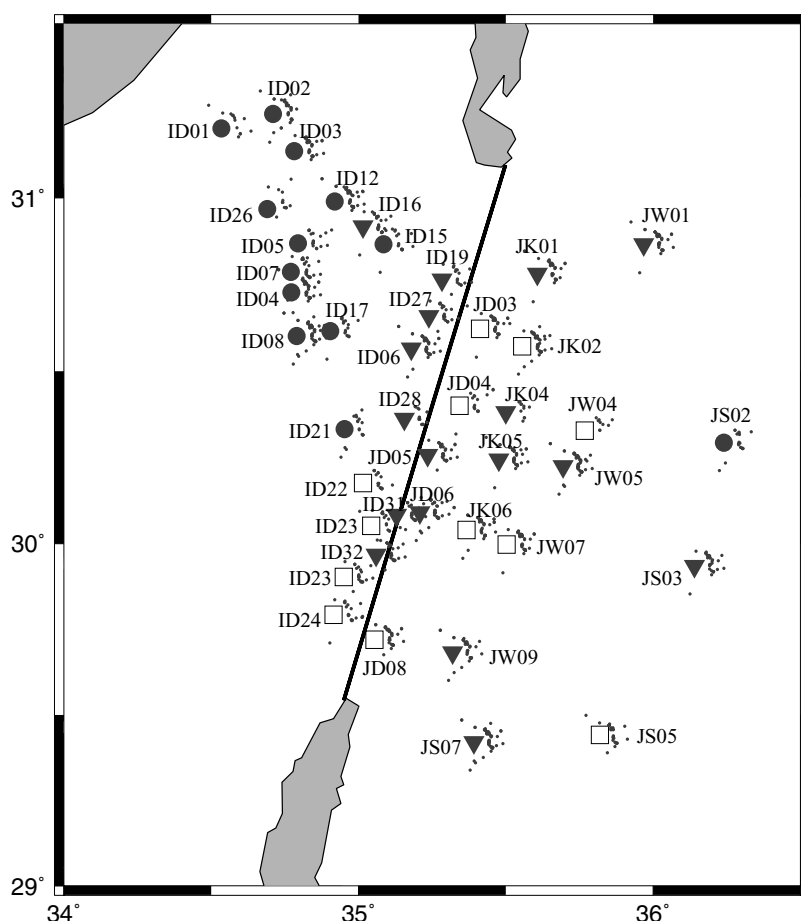


**Figure 4.** Distribution of stations of the three groups defined in Fig. 3: group A, full circles; group B, full triangles; group C, open squares. With one exception (ID16) only members of group A occur on the western side of the DST. Also with one exception (JS02) only members of groups B and C occur in the transform region or to the east of it. Piercing points at 33 km depth are shown as small dots near each station.

## CONCLUSIONS

Different seismic techniques have been applied to study the crustal structure across the Dead Sea Transform. These are steep- and wide-angle controlled-source techniques along a linear profile perpendicular to the DST and the natural source–receiver function technique in a 2-D distribution around the linear profile. The resulting Moho depth profiles agree very well in all three techniques. The Moho depths smoothly increase across the DST along the linear profile, without any indication of a sudden difference. However, an additional discontinuity in the lower crust (LCD) was identified only to the east of the DST in the receiver function and steep-angle data. This indicates that the internal crustal structure is different to the east and west of the DST and that the DST is of a deep-seated nature extending at least to the Moho. Rümpler *et al.* (2003) have concluded from anisotropy studies that the DST might reach even deeper into the upper mantle.

The smooth deepening of the Moho across the DST is, however, only observed along the controlled-source profile. The 2-D deployment of receiver function stations indicates no Moho or LCD deepening north and south of the controlled-source profile. This means that the crustal thickening across the DST towards the east may only be a local feature. East of the DST, north–south variations in the Moho depth appear to be of similar significance.

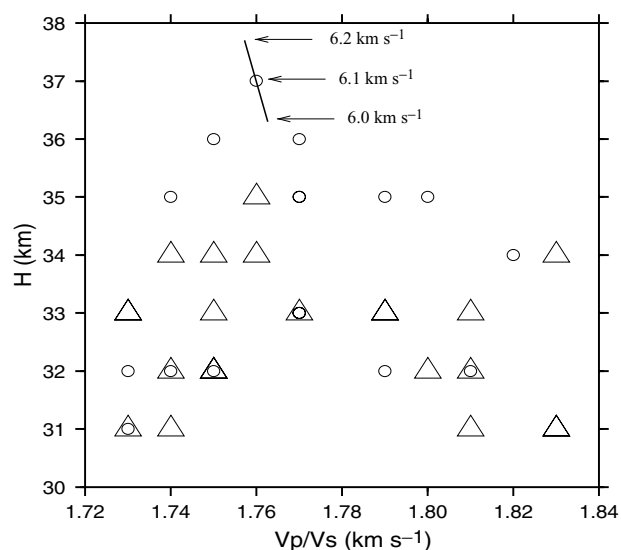


**Figure 5.** Moho depths  $H$  versus  $V_p/V_s$  ratio determined from the direct Moho conversions and their multiples using the technique of Zhu & Kanamori (2000) and an average crustal  $V_p$  of  $6.1 \text{ km s}^{-1}$  (see Table 1). Shifts of  $H$  and  $V_p/V_s$  depending on different  $V_p$  values are also indicated for one station. Open circles represent stations located on the eastern part of the DST. Stations located on the western part of the DST are represented by open triangles.

**Table 2.** Comparison of determinations of Moho depth ( $H$ ) and average  $V_p/V_s$  ratio by the method of Zhu & Kanamori (2000) (ZK) and by direct time readings of direct conversions and crustal multiples (TT). An asterisk marks stations with  $V_p/V_s$  ratios less than 1.71 or greater than 1.85. In these cases a value of 1.77 was taken.

	ID	$V_p/V_s$ (TT)	$V_p/V_s$ (ZK)	Diff.	$H$ (TT) (km)	$H$ (ZK) (km)	Diff. (km)	LCD (km)
Group A	ID02	1.74	1.74	0.00	31	32	1	
	ID01	1.75	1.74	0.01	31	31	<1	
	ID03	1.72	1.73	0.01	32	31	1	
	ID12	1.85	1.83	0.02	32	31	1	
	ID26	1.76	1.77	0.01	33	33	<1	
	ID05	1.81	1.81	0.00	32	31	1	
	ID15	1.76	1.75	0.01	32	32	<1	
	ID07	1.80	1.81	0.01	32	32	<1	
	ID04	1.77	1.75	0.02	32	32	<1	
	ID17	1.80	1.81	0.01	32	33	1	
	ID08	1.80	1.80	0.00	33	32	1	
	ID21	1.77	1.75	0.02	32	33	1	
	JS02	1.73	1.75	0.02	33	32	1	
Group B	ID16	1.92	1.83	0.09	33	31	2	21
	JW01	1.79	1.81	0.02	33	32	1	23
	JK01	1.68	1.73	0.05	31	31	<1	22
	ID19	1.77	1.76	0.01	34	35	1	23
	ID27	1.77	1.76	0.01	34	34	<1	24
	JK04	1.90	1.89* 1.77	0.01	34	35	1	25
	ID06	1.83	1.83	0.01	33	34	1	26
	ID28	1.57	1.74	0.17	32	34	2	25
	JD05	1.77	1.80	0.03	34	35	1	27
	JK05	1.76	1.79	0.03	35	35	<1	28
	JW05	1.76	1.76	0.00	37	37	<1	29
	JD06	1.76	1.75	0.01	36	36	1	27
	ID31	1.78	1.79	0.01	33	33	<1	25
	ID32	1.72	1.75	0.03	32	32	<1	23
	JS03	2.10	1.70 * 1.77	0.40	38	38	<1	23
	JW09	1.75	1.73	0.02	32	32	<1	22
	JS07	1.74	1.74	0.00	32	32	<1	23
Group C	JD03		1.79			32		
	JK02		1.67* 1.77			33		
	JD04		1.82			34		
	JW04		1.93* 1.77			36		
	ID22		1.79			33		
	ID23		1.75			34		
	JK06		1.7* 1.77			35		
	JW07		1.74			35		
	ID33		1.73			33		
	ID24		1.73			33		
	JD08		1.62* 1.77			33		
	JS05		1.77			33		

Due to the uneven distribution of distant earthquakes we only have information about the upper mantle transition zone east of the DST. The conversion times of the 410 km discontinuity are too late for a typical continental upper mantle (Li *et al.* 2003).

## ACKNOWLEDGMENTS

We thank Al-Najah National University in Nablus, Palestine, the Natural Resources Authority in Jordan and the National Ministry of Infrastructure of Israel for their support. We wish to thank Jim Mechie for reading the manuscript and for helpful comments. We also thank Dr Arthur Rodgers and one anonymous referee for their constructive reviews. The instruments were provided by the Geophysical Instrument Pool of the GeoForschungsZentrum Potsdam (GFZ). The experiment was funded by the Deutsche Forschungsgemeinschaft, the GFZ and the Minerva Dead Sea Research Centre.

Members of the DESERT Group are: M. Weber<sup>1,5</sup>, K. Abu-Ayyash<sup>2</sup>, A. Abueladas<sup>2</sup>, A. Agnon<sup>3</sup>, H. Al-Amoush<sup>1</sup>, A. Babeyko<sup>1,11</sup>, Y. Bartov<sup>4</sup>, M. Baumann<sup>5</sup>, Z. Ben-Avraham<sup>6</sup>, G. Bock<sup>1</sup>, J. Bribach<sup>1</sup>, R. El-Kelani<sup>7</sup>, A. Förster<sup>1</sup>, H.-J. Förster<sup>5</sup>, U. Frieslander<sup>8</sup>, Z. Garfunkel<sup>3</sup>, S. Grunewald<sup>1</sup>, H.J. Götze<sup>9</sup>, V. Haak<sup>1</sup>, Ch. Haberland<sup>1</sup>, M. Hassouneh<sup>2</sup>, S. Helwig<sup>10</sup>, A. Hofstetter<sup>8</sup>, K.-H. Jäkel<sup>1</sup>, D. Kesten<sup>1</sup>, R. Kind<sup>1,9</sup>, N. Maercklin<sup>1</sup>, J. Mechie<sup>1</sup>, A. Mohsen<sup>1</sup>, F.M. Neubauer<sup>10</sup>, R. Oberhänsli<sup>5</sup>, I. Qabbani<sup>2</sup>, O. Ritter<sup>1</sup>, G. Rümpler<sup>1</sup>, M. Rybakov<sup>8</sup>, T. Ryberg<sup>1</sup>, F. Scherbaum<sup>5</sup>, J. Schmidt<sup>1</sup>, A. Schulze<sup>1</sup>, S. Sobolev<sup>1</sup>, M. Stiller<sup>1</sup>, H. Thoss<sup>1</sup>, U. Weckmann<sup>1</sup>, K. Wylegalla<sup>1</sup>. Key: <sup>1</sup>GeoForschungsZentrum, Potsdam, Germany; <sup>2</sup>Natural Resources Authority, Amman, Jordan; <sup>3</sup>Hebrew University, Jerusalem; <sup>4</sup>National Ministry of Infrastructure, Jerusalem; <sup>5</sup>University of Potsdam, Germany; <sup>6</sup>Tel Aviv University, Israel; <sup>7</sup>Al-Najah National University, Nablus, Palestine; <sup>8</sup>Geophysical Institute of Israel, Lod,

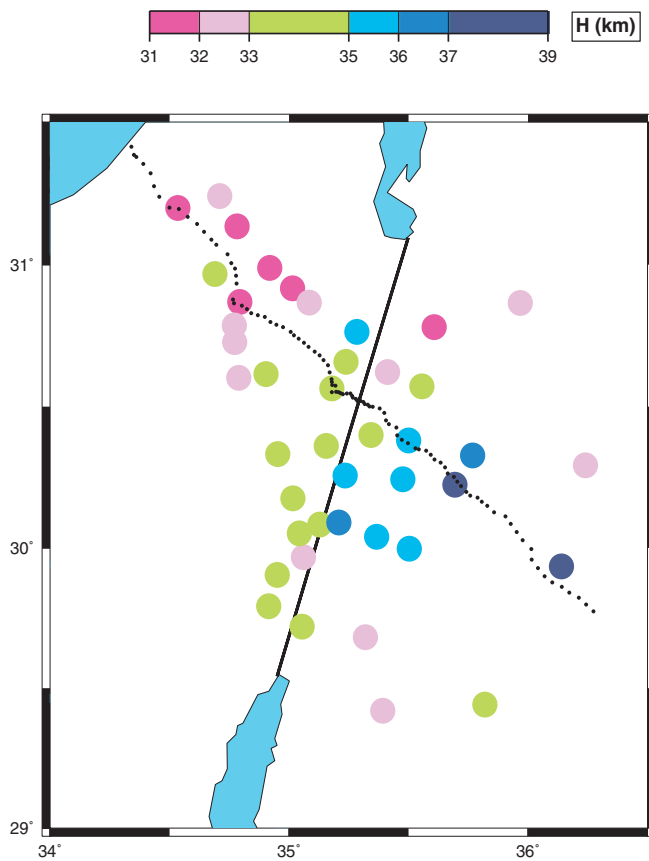


Figure 6. Map of Moho depth values from Fig. 5 and Table 1.

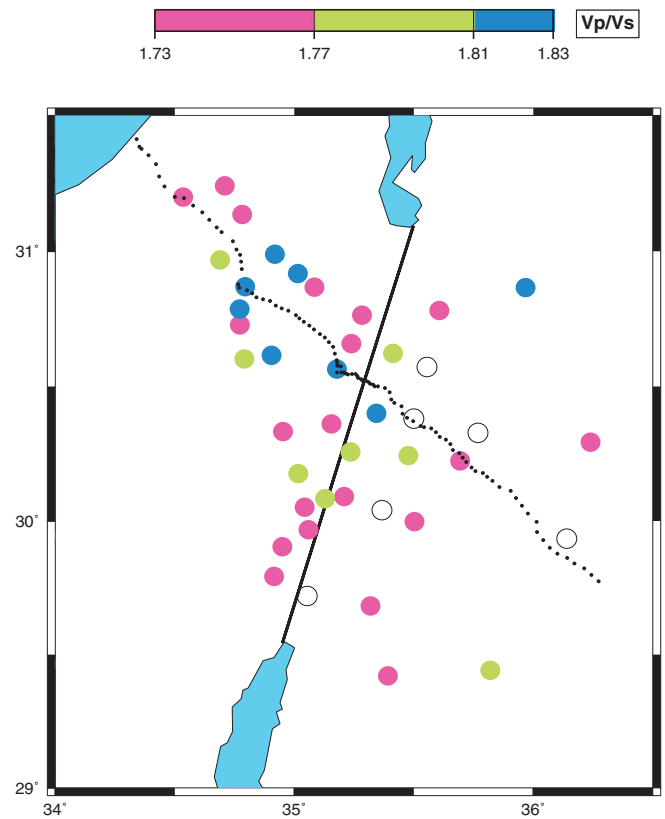


Figure 7. Map of  $V_p/V_s$  ratios from Fig. 5 and Table 1. Open circles represent stations for which the  $V_p/V_s$  ratio has not been determined.

Israel; <sup>9</sup>Free University of Berlin, Germany; <sup>10</sup>University of Köln, Germany; <sup>11</sup>Institute of Earth Physics, Moscow.

## REFERENCES

- Ammon, C.J., Randall, G.E. & Zandt, G., 1990. On the nonuniqueness of receiver function inversion, *J. geophys. Res.*, **95**, 15 303–15318.
- Burdick, L.J. & Langston, C.A., 1977. Modelling crust-structure through the use of converted phases in teleseismic body-wave-forms, *Bull. seism. Soc. Am.*, **67**, 677–691.
- DESERT Group, 2000. Multinational geoscientific research effort kicks off in the Middle East, *EOS, Trans. Am. geophys. Un.*, **81**, 609, 616–617.
- DESERT Group, 2004. The crustal structure of the Dead Sea Transform, *Geophys. J. Int.*, **156**, 655–681.
- El-Isa, Z.H., 1990. Lithospheric structure of the Jordan Dead Sea Transform from earthquake data., *Tectonophysics*, **180**, 29–36.
- Freund, R., Garfunkel, Z., Zak, I., Goldberg, M., Weissbrod, T. & Derin, B., 1970. The shear along the Dead Sea Rift, *Phil. Trans. R. Soc. Lond. A*, **267**, 107–130.
- Garfunkel, Z., 1981. Internal structure of the Dead Sea leaky transform (rift) in relation to plate kinematics, *Tectonophysics*, **80**, 81–108.
- Girdler, R.W., 1990. The Dead Sea transform fault system, *Tectonophysics*, **180**, 1–14.
- Grunewald, S., Weber, M. & Kind, R., 2001. The upper mantle under Central Europe: indications for the Eifel plume, *Geophys. J. Int.*, **147**, 590–601.
- Haberland, C. *et al.*, 2003. Modelling of seismic guided waves at the Dead Sea Transform, *J. geophys. Res.*, **108**(B7), 2342, doi:10.1029/2002JB002309.
- Helffrich, G., 2000. Topography of the transition zone seismic discontinuities, *Rev. Geophys.*, **38**, 141–158.
- Hofstetter, R. & Bock, G., 2004. Shear-wave velocity structure of the Sinai sub-plate from receiver function analysis, *Geophys. J. Int.*, **158**, 67–84.
- Kind, R., Kosarev, G.L. & Petersen, N.V., 1995. Receiver functions at the stations of the German Regional Seismic Network (GRSN), *Geophys. J. Int.*, **121**, 191–202.
- Kind, R. *et al.*, 2002. Seismic images of crust and upper mantle beneath Tibet: evidence for Eurasian plate subduction, *Science*, **298**, 1219–1221.
- Kosarev, G., Kind, R., Sobolev, S.V., Yuan, X., Hanka, W. & Oreshin, S., 1999. Seismic evidence for a detached Indian lithospheric mantle beneath Tibet, *Science*, **283**, 1306–1309.
- Koulakov, I., Oreshin, S., Sobolev, S.V. & Hofstetter, R., 2004. *P* velocity anomalies in the upper mantle beneath the Dead Sea Transform and adjacent regions from teleseismic tomography, *Geophys. J. Int.*, submitted.
- Kovach, R., Andreason, G., Gettings, M. & El-Kaysi, K., 1990. Geophysical investigations in Jordan, *Tectonophysics*, **180**, 61–69.
- Langston, C.A., 1994. An integrated study of crustal structure and regional wave propagation for southeastern Missouri, *Bull. seism. Soc. Am.*, **84**, 105–118.
- Li, X., Kind, R., Yuan, X., Sobolev, S.V., Hanka, W., Ramesh, D.S., Gu, Y. & Dziewonski, A.M., 2003. Seismic observation of narrow plumes in the oceanic upper mantle, *Geophys. Res. Lett.*, **30**(6), doi:10.1029/2002GL015411.
- McKenzie, D., 1972. Active tectonics of the Mediterranean region, *Geophys. J. R. astr. Soc.*, **30**, 109–185.
- McKenzie, D., Davies, D. & Molnar, P., 1970. Plate tectonics of the Red Sea and East Africa, *Nature*, **226**, 243–248.
- Mechie, J., Abu-Ayyash, K., Ben-Avraham, Z., El-Kelani, R., Mohsen, A., Rümpker, G., Saul, J. & Weber, M., 2004. Crustal shear velocity structure across the Dead Sea Transform from 2-D modelling of project DESERT explosion seismic data, *Geophys. J. Int.*, in press.
- Nyblade, A.A., Knox, R.P. & Gurrrola, H., 2000. Mantle transition zone thickness beneath Afar: implications for the origin of the Afar hotspot, *Geophys. J. Int.*, **142**, 615–619.

- Owens, T.J., Zandt, G. & Taylor, S.R., 1984. Seismic evidence for an ancient rift beneath the Cumberland Plateau, Tennessee: a detailed analysis of broadband teleseismic *P* waveforms, *J. geophys. Res.*, **89**, 7783–7795.
- Owens, T. J., Nyblade, A.A., Gurrola, H. & Langston, C.A., 2000. Mantle transition zone structure beneath Tanzania, East Africa, *Geophys. Res. Lett.*, **27**, 827–830.
- Quennell, A.M., 1958. The structural and geomorphic evolution of the Dead Sea Rift, *Q. J. geol. Soc. Lond.*, **114**, 2–24.
- Ramesh, D.S., Kind, R. & Yuan, X., 2002. Receiver function analysis of the North American crust and upper mantle, *Geophys. J. Int.*, **150**, 91–108.
- Rümpker, G., Ryberg, T., Bock, G. & DESERT Group, 2003. Evidence for boundary layer mantle flow beneath the Dead Sea Transform from seismic anisotropy, *Nature*, **425**, 497–501.
- Sandvol, E., Seber, D., Calvert, A. & Barazangi, M., 1998. Grid search modelling of receiver functions: implications for crustal structure in the Middle East and North Africa, *J. geophys. Res.*, **103**, 26 899–26 917.
- Sobolev, S.V., Garfunkel, Z., Babeyko, A.Yu., Petrunin, A. & DESERT Interpretation Group, 2004. Thermo-mechanical model of the Dead Sea Transform, *Earth Planet. Sci. Lett.*, submitted.
- Vinnik, L.P., 1977. Detection of waves converted from *P* to *SV* in the mantle, *Phys. Earth planet. Int.*, **15**, 39–45.
- Wilson, T., 1965. A new class of faults and their bearing on continental drift, *Nature*, **4995**, 343–347.
- Yuan, X., Ni, J., Kind, R., Mechie, J. & Sandvol, E., 1997. Lithospheric and upper mantle structure of southern Tibet from a seismological passive source experiment, *J. geophys. Res.*, **102**, 27 491–27 500.
- Yuan, X. *et al.*, 2000. Subduction and collision processes in the Central Andes constrained by converted seismic phases, *Nature*, **408**, 958–961.
- Yuan, X., Sobolev, S.V. & Kind, R., 2002. Moho topography in the central Andes and its geodynamic implications, *Earth planet. Sci. Lett.*, **199**, 389–402.
- Zandt, G. & Ammon, C.J., 1995. Continental crust composition constrained by measurements of crustal Poisson's ratio, *Nature*, **374**, 152–154.
- Zandt, G., Myers, S.C. & Wallace, T.C., 1995. Crustal and mantle structure across the Basin and Range—Colorado Plateau boundary at 37°N latitude and implications for Cenozoic extensional mechanism, *J. geophys. Res.*, **100**, 10 529–10 548.
- Zhu, H. & Kanamori, H., 2000. Moho depth variation in southern California from teleseismic receiver functions, *J. geophys. Res.*, **105**, 2969–2980.

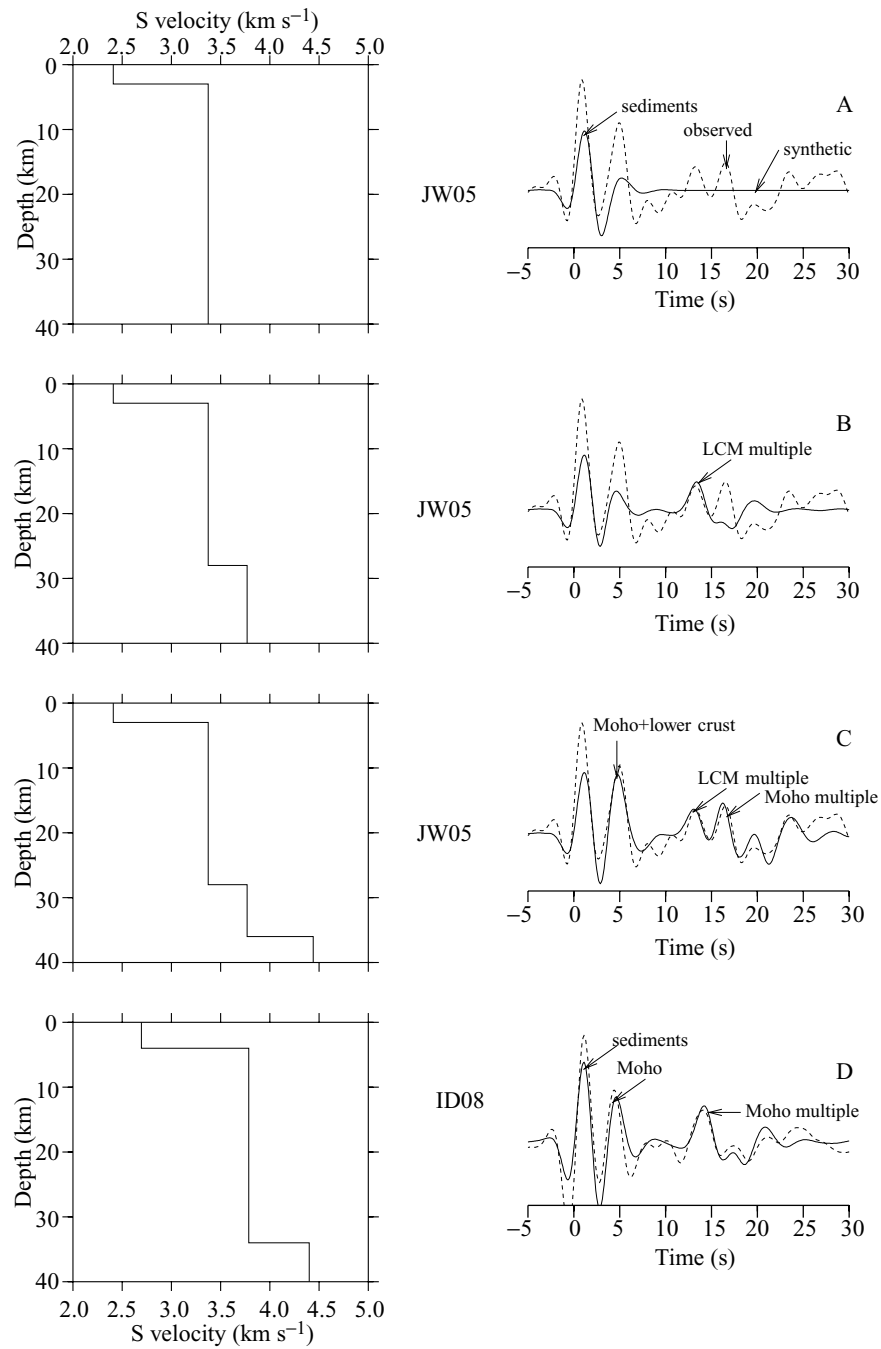


**Figure 8.** Waveform modelling of one station east (JW05, A–C) and one station west (ID08, D) of the DST. The left panels show the final model, whereas in the right panels the computed waveforms (continuous lines) and the observed waveforms (dashed lines) are shown. The Moho depth is 37 and 33 km at stations JW05 and ID08, respectively. The Lower Crustal Discontinuity at station JW05 (east of the DST) is at 29 km depth.

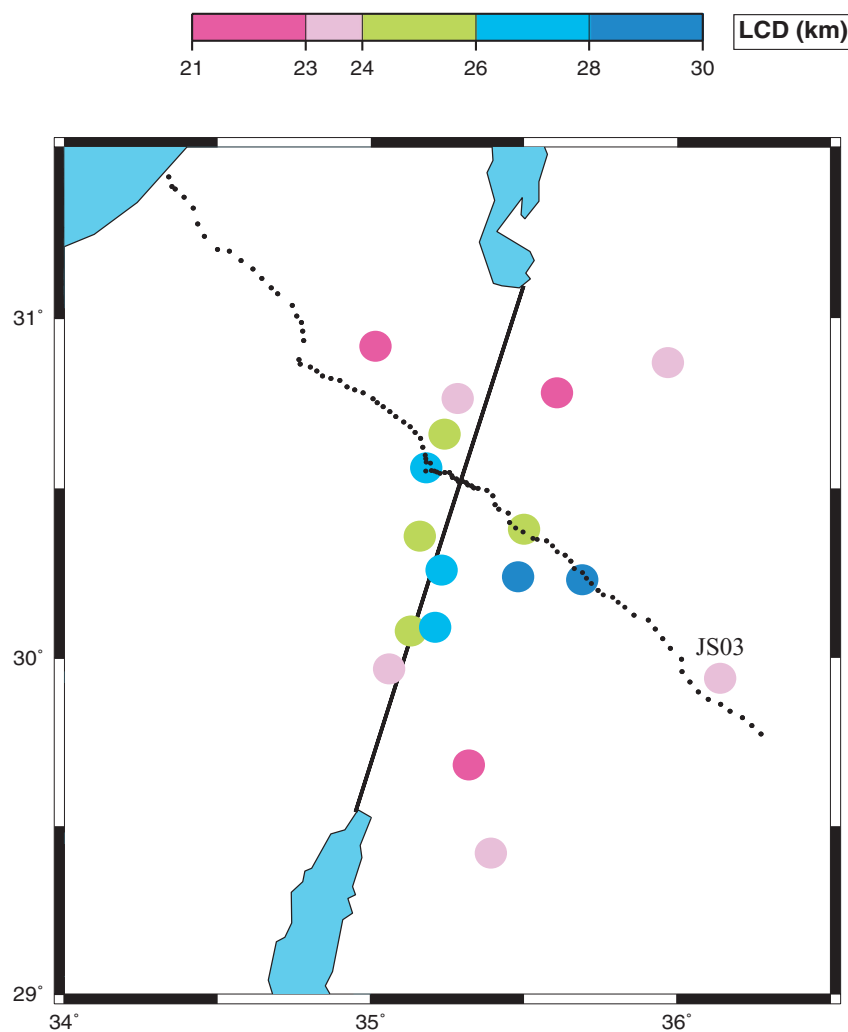


**Figure 9.** Map of the Lower Crustal Discontinuity (LCD) occurring mainly east of the Dead Sea Transform. The LCD is deepest near the controlled-source line except for station JS03. At the northern and southern ends of the station network the LCD is shallower again.

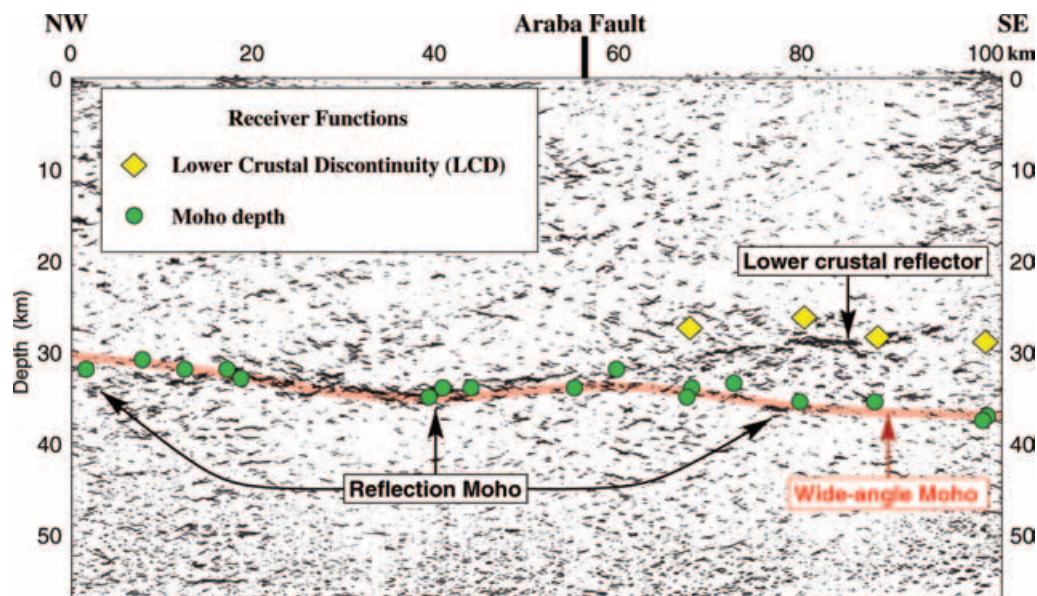


**Figure 10.** Comparison of depth determinations of the Moho and Lower Crustal Discontinuity by steep- and wide-angle controlled-source techniques and receiver functions. The error in the Moho depth determined with receiver functions is estimated at less than 1 km at most stations (see Table 2).

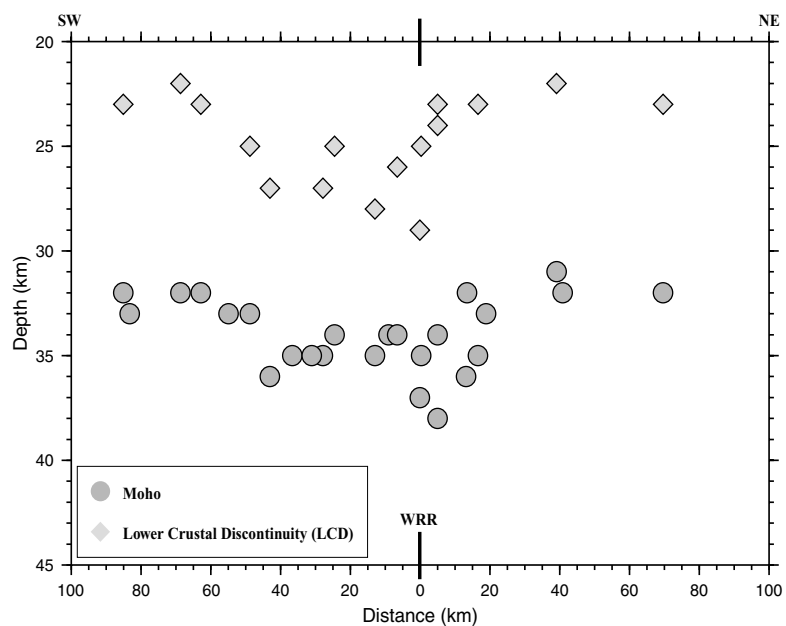


**Figure 11.** Projection of depths of the Moho and Lower Crustal Discontinuity (LCD) at and east of the DST on a southwest to northeast profile perpendicular to the controlled-source profile. Both the Moho and the LCD are unusually deep exactly at the location of the controlled-source profile (WRR at 0 km).

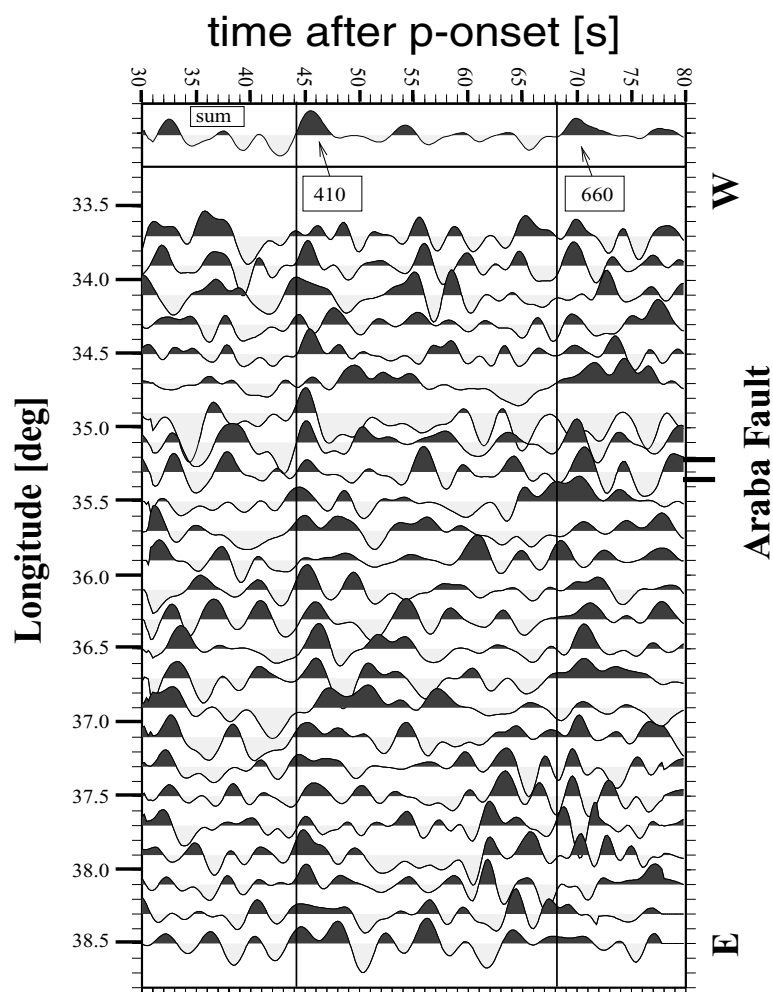


**Figure 12.** Observations of conversions from the 410 and 660 km discontinuities in the DESERT experiment. The 410 km discontinuity is clearly seen, while the 660 km one is poorly imaged.

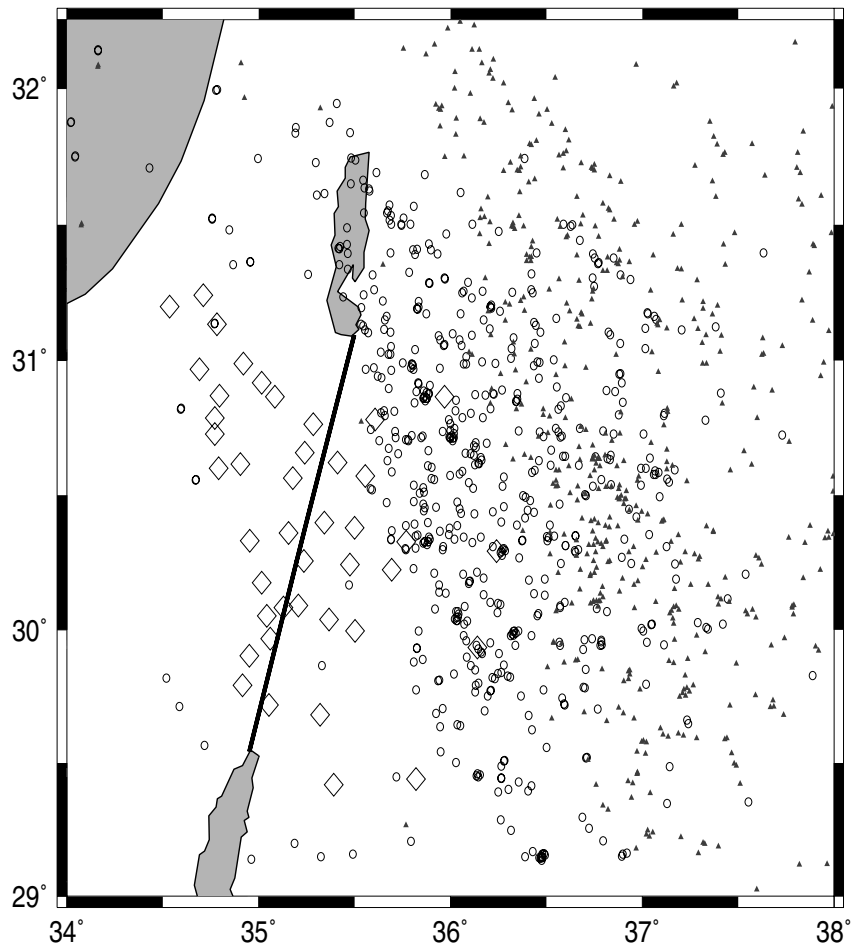


**Figure 13.** Distribution of piercing points at the 410 km (open circles) and 660 km (filled triangles) discontinuities. Open diamonds are station locations. Practically all piercing points are east of the DST. Therefore we have no information about the mantle transition zone across the DST.